Available online at www.sciencedirect.com
SCIENCE DIRECT®
ELSEVIER
European Journal of Mechanics B/Fluids 22 (2003) 105–121

On the relationship between the pressure and the projection function in the numerical computation of viscous incompressible flow ☆

C. Pozrikidis

Department of Mechanical and Aerospace Engineering, University of California, San Diego, La Jolla, CA 92093-0411, USA

Received 12 August 2002; received in revised form 10 December 2002; accepted 26 February 2003

Abstract

The relationship between the pressure p and the projection function ϕ employed in the numerical computation of viscous incompressible flow using the fractional-step method is discussed. To leading order, the difference $p - \phi$ is proportional to the divergence of the intermediate velocity, $\mathbf{u}^*$, computed by integrating the equation of motion in the absence of the pressure gradient. Previous authors have shown that the intermediate rate of expansion, $\alpha^* \equiv \nabla \cdot \mathbf{u}^*$ is supported by numerical boundary-layers of thickness $\delta \simeq (\nu \Delta t)^{1/2}$, where Δt is the time step and ν is the kinematic viscosity. We demonstrate that, in the absence of singularities due to discontinuous boundary velocity, the magnitude of α^* changes by an amount of order δ across the boundary layers and of higher order in the bulk of the flow, and argue that adding a computable correction to the projection function allows us to recover the pressure with temporal accuracy whose order matches that of the method used for carrying out the convection–diffusion step. When the boundary velocity is discontinuous, the normal derivative of the pressure exhibits strong singularities, and the computation of the pressure using finite-difference methods on non-staggered grids is notably sensitive to the numerical implementation. In contrast, in spite of the singular behavior of the intermediate rate of expansion, the solution of the Poisson equation for the projection function subject to the homogeneous Neumann boundary condition is less sensitive to the numerical method. Computing the projection function thus emerges as a preferred venue of approximating the pressure on non-staggered grids even under demanding conditions.

Keywords: Incompressible flow; Viscous flow; Projection methods; Finite-difference methods; Driven cavity flow

1. Introduction

The equation of motion for a viscous incompressible fluid states that the velocity at a particular point in a flow changes by four contributions: the nonlinear inertial acceleration force, the pressure force, the viscous force, and the body force. In the fractional-step method, selected groups of these terms are decoupled and considered to act in a sequential fashion over repeated small periods of elapsed time. Chorin's projection method is based on the idea that the change due to the pressure gradient may be implemented in terms of an instantaneous projection whose role is to receive the velocity field delivered by all other contributions, and remove the non-solenoidal component in a way that is consistent with the boundary conditions [1,2]. In practice, the projection step for a fluid with uniform density is carried out by decomposing the intermediate velocity at the end of the convection–diffusion and body-force steps into an irrotational and a solenoidal component, and identifying the latter with the physical velocity evaluated at the new time level. Thus, the projection step preserves the vorticity of the intermediate flow, which is consistent with the absence of baroclinic production of vorticity. In the numerical implementation, the irrotational

☆ This research has been supported by a grant provided by the National Science Foundation.
E-mail address: cpozrikidis@ucsd.edu (C. Pozrikidis).
URL address: http://stokes.ucsd.edu/pozrikidis.

0997-7546/03/$ – see front matter
doi:10.1016/S0997-7546(03)00021-9

component is set equal to the gradient of a projection function ϕ that is related, but is not identical, to the hydrodynamic pressure p.

Numerous variations of the projection method have been developed in the past three decades in the form of (a) pressure-correction or pressure-update methods where the velocity is advanced by the gradient of an approximate extrapolated pressure and the projection step makes a correction, and (b) pure projection methods where the pressure field is abandoned altogether in favor of the projection function, as discussed in the previous paragraph (e.g., [3–9]). However, Chorin's concept of an instantaneous projection into the space of solenoidal vector functions is a key idea in all implementations. Despite the voluminous relevant literature, the relation between the projection function and the physical pressure has received only scant attention and remains controversial and unclear (e.g., [10,3,11–14]).

In comparing the projection function with the pressure, we observe that the former satisfies boundary conditions that are determined by the choice of boundary conditions for the intermediate velocity at the end of the convection–diffusion and body-force steps (e.g., [4,5]), whereas the pressure satisfies unambiguous boundary conditions arising by projecting the equation of motion normal to the boundaries and simplifying the resulting expressions using the specified physical boundary conditions (e.g., [15]). In particular, pure projection methods typically require that the intermediate velocity satisfies the non-penetration boundary condition; accordingly, the projection function obeys the homogeneous Neumann boundary condition. Although the difference between the Neumann boundary conditions satisfied by the projection function and the pressure is typically of order unity, the difference of the functions themselves, $p-\phi$, evaluated at appropriate time levels, is proportional to the divergence of the intermediate velocity, which changes by an amount of order $\delta \simeq (\nu\Delta t)^{1/2}$ across numerical boundary layers of comparable thickness [16,17,13]. The existence of intermediate numerical boundary layers for the rate of expansion was first pointed out by Orszag et al. [18] in the context of the pressure Poisson equation. In Section 2 of this paper, we shall show that, far from the boundaries, the difference $p-\phi$ decays to zero in the case of unforced Stokes flow, and is of first or second order in Δt under more general conditions. Consequently, in the limit as Δt tends to zero, the projection function tends to the pressure in the vicinity, as well as far from the boundaries.

Several authors have expressed the opinion that, because of the splitting of the convection–diffusion and projection steps, projection methods are inherently first-order accurate in time for the pressure, although they can readily be designed to be second-order accurate for the velocity. For example, a second-order method for the velocity arises by carrying out the convection–diffusion step using a second-order method that involves Adams–Bashforth and Crank–Nicolson discretization, respectively, for the convective and diffusive contributions. Lee et al. [19] review a class of second-order methods for the velocity developed in the framework of block factorization. Recently, it was pointed out that the accuracy of the pressure can be improved by setting $p=\phi-\chi$, where p and ϕ are evaluated at appropriate time levels, and the leading-order contribution to the computable correction, χ, is proportional to the intermediate rate of expansion [14]. In particular, if the numerical method used to carry out the convection–diffusion step is of second-order in the time step, then adding the computable correction yields the pressure with a commensurate second-order accuracy. In this paper, we shall enhance and complete this argument, and shall further point out that failure to satisfy the continuity equation to machine accuracy may introduce an unaccountable source of error.

The preceding discussion applies only when the pressure field is nonsingular throughout the domain of flow and over the boundaries. Consider the classical problem of flow in a cavity driven by the translation of a rigid lid. An analysis of the flow near the corners where the velocity is discontinuous reveals that the pressure and its normal derivative exhibit strong singularities. In the extreme case of Stokes flow, the pressure Poisson equation reduces to Laplace's equation, and the solution is forced by two point-source dipoles located at the singular points. In Section 4, we shall present numerical results to demonstrate that, in spite of the corner singularities, the projection function is computed reliably using standard finite-difference methods on non-staggered grids. In contrast, the computation of the pressure using finite-difference methods on non-staggered grids is notably sensitive to the numerical implementation. This significant difference in performance places the projection function in a superior position and advocates its usage as a convenient venue for approximating the pressure even under demanding conditions.

2. Analysis of a pure projection method

Consider the unsteady flow of an incompressible Newtonian fluid with uniform density and viscosity in a domain that is bounded exclusively by surfaces where the no-penetration and no-slip boundary conditions are required. The motion of the fluid is governed by the Navier–Stokes equation

$$\rho\frac{\partial \mathbf{u}}{\partial t} = \rho\mathbf{N} - \nabla p + \mu\nabla^2\mathbf{u} + \rho\mathbf{f}, \tag{2.1}$$

and the continuity equation

$$\nabla\cdot\mathbf{u} = 0, \tag{2.2}$$

where is ρ is the fluid density, μ is the fluid viscosity, $\mathbf{u}$ is the velocity, p is the pressure $\mathbf{N} = -\mathbf{u}\cdot\nabla\mathbf{u}$ the nonlinear part of the fluid particle acceleration, and $\mathbf{f}$ is the acceleration due to a distributed force field such as gravity (e.g., [15]). The system of governing equations (2.1) and (2.2) must be accompanied by: (a) an initial condition that specifies the velocity at the interior of the flow denoted by Ω and along the boundaries Γ, $\mathbf{u}(\mathbf{x}, t=0) \equiv \mathbf{u}_0$, and (b) a boundary condition that specifies the boundary distribution of the velocity at all times $\mathbf{u}(\mathbf{x}, t) = \mathbf{u}_B(\mathbf{x}, t)$, where $\mathbf{x}$ lies on Γ.

To develop the projection method, we regard the equation of motion (2.1) as an evolution equation for the velocity, and split the operator on the right-hand side into a convection–diffusion component incorporating the body force, and a companion projection component (e.g., [20]). In their pure forms, the constituent equations are

$$\rho\frac{\partial\mathbf{u}}{\partial t} = \rho\mathbf{N} + \mu\nabla^2\mathbf{u} + \rho\mathbf{f}, \tag{2.3}$$

and

$$\rho\frac{\partial\mathbf{u}}{\partial t} = -\nabla\phi. \tag{2.4}$$

Eq. (2.3) receives the velocity field at time t^n, and advances it over a time interval Δt to the intermediate distribution $\mathbf{u}^*$. Subsequently, Eq. (2.4) receives the intermediate velocity field and advances it over the same time period to the final value $\mathbf{u}^{n+1}$, thereby completing the execution of a step. Because it is not clear that the projection function ϕ is equal to the pressure p, it has been denoted by a different symbol. The key idea of the projection method is that ϕ should be computed so that the final velocity field $\mathbf{u}^{n+1}$ is solenoidal, as required by the continuity equation (2.2).

To carry out the first step according to (2.3), we require boundary conditions for the intermediate velocity. A consistent set of boundary conditions include the Dirichlet boundary condition for the normal and tangential components of the velocity

$$\begin{aligned}
&\mathbf{u}^*\cdot\mathbf{n} = \mathbf{u}_B^{n+1}\cdot\mathbf{n},\\
&\mathbf{u}^*\cdot\mathbf{t} = \left(\mathbf{u}_B^{n+1} + \frac{1}{\rho}\int_{t^n}^{t^n+\Delta t}\nabla\phi\,\mathrm{d}t\right)\cdot\mathbf{t},
\end{aligned} \tag{2.5}$$

where $\mathbf{n}$ and $\mathbf{t}$ are unit vectors normal and tangent to the boundary Γ. Correspondingly, the projection function satisfies the homogeneous Neumann condition

$$\mathbf{n}\cdot\int_{t^n}^{t^n+\Delta t}\nabla\phi\,\mathrm{d}t = 0. \tag{2.6}$$

Straightforward substitution demonstrates that (2.5) and (2.6) ensure the required boundary condition $\mathbf{u}^{n+1} = \mathbf{u}_B^{n+1}$ at the end of a complete step. In expressions (2.5) and (2.6), the projection function is regarded as a continuous function of time over the interval where Eq. (2.4) applies. In numerical practice, the continuous evolution is replaced by an instantaneous projection.

Evolution equations for the rate of expansion $\alpha \equiv \nabla\cdot\mathbf{u}$ arise by taking the divergence of (2.3) and (2.4), finding

$$\rho\frac{\partial\alpha}{\partial t} = \rho\nabla\cdot(\mathbf{N}+\mathbf{f}) + \mu\nabla^2\alpha, \tag{2.7}$$

and

$$\rho\frac{\partial\alpha}{\partial t} = -\nabla^2\phi. \tag{2.8}$$

The component equation (2.7) receives the presumed vanishing rate of expansion at the time level t^n, and advances it over the time interval Δt to the intermediate distribution α^*. The projection component equation (2.8) then receives α^* and advances it over the same time interval to the final distribution α^{n+1}, which is required to vanish throughout the domain of flow and over the boundaries.

2.1. Time-discretized equations

The temporal discretization of Eqs. (2.3) and (2.7) according to the generalized Crank–Nicolson method yields the semi-discrete forms

$$\rho\frac{\mathbf{u}^*-\mathbf{u}^n}{\Delta t} = \rho(\mathbf{N}+\mathbf{f})^{n+\gamma} + \mu\left[(1-\gamma)\nabla^2\mathbf{u}^n + \gamma\nabla^2\mathbf{u}^*\right] \tag{2.9}$$

and

$$\rho\frac{\alpha^*-\alpha^n}{\Delta t}=\rho\big[\nabla\cdot(\mathbf{N}+\mathbf{f})\big]^{n+\gamma}+\mu\big[(1-\gamma)\nabla^2\alpha^n+\gamma\nabla^2\alpha^*\big], \tag{2.10}$$

where the numerical parameter γ varies in $(0,1]$. The term $(\mathbf{N}+\mathbf{f})^{n+\gamma}$ is assumed to be available with $\mathrm{O}(\Delta t^m)$ accuracy in terms of the *extrapolated* or *interpolated* velocity of the *physical* flow and body force evaluated at time $t^n+\gamma\Delta t$, where $m=2$ for a second-order method.

Rearranging (2.10), we derive an inhomogeneous Helmholtz equation for the intermediate rate of expansion,

$$\alpha^*-\gamma\nu\Delta t\nabla^2\alpha^*=\Delta t\big[\nabla\cdot(\mathbf{N}+\mathbf{f})\big]^{n+\gamma}+R_+^n, \tag{2.11}$$

where $\nu\equiv\mu/\rho$ is the kinematic viscosity, and $R_+^n\equiv\alpha^n+(1-\gamma)\nu\Delta t\nabla^2\alpha^n$. In the temporal semi-discrete formulation presently considered, R_+ vanishes throughout the domain of flow and along the boundaries. In a full time-space discretization, R_+ vanishes to machine accuracy only for a certain class of craftily designed numerical methods [21].

Turning now to the projection step, we replace (2.4) and (2.8) with the time discretized equations

$$\rho\frac{\mathbf{u}^{n+1}-\mathbf{u}^*}{\Delta t}=-\nabla\phi^{n+1} \tag{2.12}$$

and

$$\rho\frac{\alpha^{n+1}-\alpha^*}{\Delta t}=-\nabla^2\phi^{n+1}. \tag{2.13}$$

Solving (2.13) for α^*, we obtain

$$\alpha^*=\alpha^{n+1}+\frac{\Delta t}{\rho}\nabla^2\phi^{n+1}. \tag{2.14}$$

Requiring that $\alpha^{n+1}=0$, we derive a Poisson equation for ϕ^{n+1},

$$\nabla^2\phi^{n+1}=\frac{\rho}{\Delta t}\alpha^*, \tag{2.15}$$

which is to be solved subject to the homogeneous Neumann condition $\mathbf{n}\cdot\nabla\phi^{n+1}=0$ originating from (2.6).

Substituting now the right-hand side of (2.14) for α^* in (2.11) and rearranging, we find

$$\nabla^2\big(\phi^{n+1}-\gamma\nu\Delta t\nabla^2\phi^{n+1}\big)=\rho\big[\nabla\cdot(\mathbf{N}+\mathbf{f})\big]^{n+\gamma}-\frac{\rho}{\Delta t}\big(R_-^{n+1}-R_+^n\big). \tag{2.16}$$

The residual $R_-^{n+1}\equiv\alpha^{n+1}-\gamma\nu\Delta t\nabla^2\alpha^{n+1}$ vanishes precisely in the space-continuous formulation presently considered, and approximately in a discrete spatial implementation.

2.2. Relationship between the projection function and the pressure

To deduce the relation between the projection function and the pressure, we take the divergence of the equation of motion (2.1) and enforce the incompressibility condition (2.2) to derive the pressure Poisson equation. Applying this equation at time $t^{n+\gamma}$, we obtain

$$\nabla^2 p^{n+\gamma}=\rho\big[\nabla\cdot(\mathbf{N}+\mathbf{f})\big]_E^{n+\gamma}, \tag{2.17}$$

where the subscript E denotes the exact value. Subtracting (2.16) from (2.17) and rearranging, we find

$$\begin{aligned}&\nabla^2\big(p^{n+\gamma}-\phi^{n+1}+\gamma\nu\Delta t\nabla^2\phi^{n+1}\big)+\rho\big[\big[\nabla\cdot(\mathbf{N}+\mathbf{f})\big]^{n+\gamma}-\big[\nabla\cdot(\mathbf{N}+\mathbf{f})\big]_E^{n+\gamma}\big]\\&\quad=\frac{\rho}{\Delta t}\big(R_-^{n+1}-R_+^n\big)=\rho\left(\frac{\alpha^{n+1}-\alpha^n}{\Delta t}-\nu\big[(1-\gamma)\nabla^2\alpha^n+\gamma\nabla^2\alpha^{n+1}\big]\right).\end{aligned} \tag{2.18}$$

By definition, the expression enclosed by the square brackets on the left-hand side is of $\mathrm{O}(\Delta t^m)$.

In the space-continuous formulation, $\alpha^n=0$ and $\alpha^{n+1}=0$, the right-hand side of (2.18) vanishes, and the expression enclosed by the first set of parentheses on the left-hand side of (2.18) is a harmonic function up to $\mathrm{O}(\Delta t^m)$, denoted by χ. Rearranging, we find

$$p^{n+\gamma}=\phi^{n+1}-\gamma\nu\Delta t\nabla^2\phi^{n+1}+\chi+\mathrm{O}\big(\Delta t^m\big)=\phi^{n+1}-\gamma\mu\alpha^*+\chi+\mathrm{O}\big(\Delta t^m\big). \tag{2.19}$$

Neumann boundary conditions for χ arise by projecting the gradient of (2.19) normal to the boundaries of the flow. Using the equation of motion (2.1) and the homogeneous Neumann boundary condition for ϕ^{n+1}, we find

$$\mathbf{n}\cdot\nabla\chi = \mathbf{n}\cdot\left[-\rho\left(\frac{\partial \mathbf{u}_B}{\partial t}\right)^{n+\gamma} + \rho(\mathbf{N}+\mathbf{f})_E^{n+\gamma} + \mu\big(\nabla^2\mathbf{u}\big)_E^{n+\gamma} + \gamma\nu\Delta t\nabla\big(\nabla^2\phi^{n+1}\big)\right] + \mathrm{O}\big(\Delta t^m\big). \tag{2.20}$$

Next, we substitute the approximation

$$\big(\nabla^2\mathbf{u}^{n+\gamma}\big)_E = (1-\gamma)\nabla^2\mathbf{u}^n + \gamma\nabla^2\mathbf{u}^{n+1} + \mathrm{O}\big(\Delta t^l\big) \tag{2.21}$$

into the right-hand side of (2.20), where l is the temporal order of the physical velocity. Using (2.9) and the Laplacian of (2.12) to eliminate the Laplacian of the velocity, we finally find

$$\mathbf{n}\cdot\nabla\chi = \rho\mathbf{n}\cdot\left[\frac{\mathbf{u}^*-\mathbf{u}^n}{\Delta t} - \left(\frac{\partial \mathbf{u}_B}{\partial t}\right)^{n+\gamma} + \mathrm{O}\big(\Delta t^l\big) + \mathrm{O}\big(\Delta t^m\big)\right]. \tag{2.22}$$

In view of the first of the boundary conditions (2.5), the right-hand side of (2.22) vanishes up to order $\Delta t^m + \Delta t^l$, and the harmonic function χ is constant within this precision. Eq. (2.19) then yields

$$p^{n+\gamma} = \phi^{n+1} - \gamma\nu\Delta t\nabla^2\phi^{n+1} + \mathrm{O}\big(\Delta t^l\big) + \mathrm{O}\big(\Delta t^m\big) = \phi^{n+1} - \gamma\mu\alpha^* + \mathrm{O}\big(\Delta t^l\big) + \mathrm{O}\big(\Delta t^m\big). \tag{2.23}$$

In the case of the Crank–Nicolson discretization corresponding to $\gamma = 1/2$ and $l = 2$, and an interpolation or extrapolation method for the nonlinear term corresponding to $m = 2$, we obtain

$$p^{n+\frac{1}{2}} = \phi^{n+1} - \frac{1}{2}\nu\Delta t\nabla^2\phi^{n+1} + \mathrm{O}\big(\Delta t^2\big) = \phi^{n+1} - \frac{1}{2}\mu\alpha^* + \mathrm{O}\big(\Delta t^2\big), \tag{2.24}$$

in agreement with the results of previous authors [14,10].

Relation (2.23) can be inferred directly by using (2.12) to eliminate the intermediate velocity from (2.9), obtaining

$$\rho\frac{\mathbf{u}^{n+1}-\mathbf{u}^n}{\Delta t} = \rho(\mathbf{N}+\mathbf{f})^{n+\gamma} - \nabla\big(\phi^{n+1} - \gamma\mu\alpha^*\big) + \mu\big[(1-\gamma)\nabla^2\mathbf{u}^n + \gamma\nabla^2\mathbf{u}^{n+1}\big]. \tag{2.25}$$

Comparing this expression with the equation of motion discretized according to the generalized Crank–Nicolson method, shows that second order temporal accuracy for the velocity is achieved when $\gamma = 1/2$, the pressure is evaluated according to (2.24), and the nonlinear term is evaluated with second order accuracy by extrapolation or interpolation [14,10]. The preceding derivation based on the Poisson equation, however, ensures that the replacing the continuity equation with Poisson's equations (2.15) and (2.17) preserves the equivalence.

2.3. Boundary layers of the intermediate rate of expansion

Consider the case of unsteady Stokes flow occurring in the absence of a distributed body force. In the space-continuous formulation, (2.11) reduces to the homogeneous equation

$$\alpha^* - \gamma\nu\Delta t\nabla^2\alpha^* = 0. \tag{2.26}$$

Balancing the magnitude of the first two terms on the left-hand side, we find that the intermediate rate of expansion α^* is supported by boundary layers of thickness $\delta \simeq (\gamma\nu\Delta t)^{1/2}$. As γ tends to zero yielding an explicit discretization, the thickness of the boundary layer vanishes and the numerical method fails. According to (2.23), the normal derivative of α^* at the boundary must be comparable to the normal derivative of the pressure, and this requires that, inside the boundary layer, α^* is of order δ. Correspondingly, the second term on the right-hand side of (2.23) makes a leading-order contribution of order δ inside the boundary layer, and decays in an exponential fashion outside the boundary layer, in agreement with previous theoretical analysis [17,3,13]. Under more general conditions of unsteady Navier–Stokes flow and in the presence of a distributed body force, the right-hand side of (2.11) is significant throughout the domain of flow, and α^* is of order Δt in the interior of the flow and varies by an amount of order $\Delta t^{1/2}$ across the boundary layers.

In the fully-discrete time-space implementation, the right-hand side of (2.18) does not generally vanish to machine accuracy, and is of order $\Delta t \times h^m$, where the exponent m depends on the spatial discretization. Accordingly, the right-hand sides of (2.23) and (2.24) are enhanced with corrections that may lower the nominal order of the numerical method.

3. Numerical methods

To confirm the theoretical predictions and investigate the significance of boundary singularities, we consider two-dimensional flow in a rectangular cavity of size $L_x \times L_y$, as illustrated in Fig. 1, subject to a prescribed tangential lid velocity,

$$u_x^{\text{lid}}(x,t) = Uf(t)g(x), \tag{3.1}$$

where U is the maximum lid velocity, $0 \leqslant x \leqslant L_x$, and $0 \leqslant y \leqslant L_y$. The dimensionless functions $f(t)$ and $g(x)$ determine, respectively, the temporal behavior and spatial distribution of the lid velocity. The Reynolds number is defined as $Re = UL_x/\nu$.

Two types of motion are considered: flow due to impulsive lid translation corresponding to $f(t) = H(t)$, where $H(t)$ is the Heaviside step function, and flow due to ramped lid translation corresponding to $f(t) = 1 - \exp(-t\nu/(\tau L_y^2))$, where τ is a dimensionless time constant expressing the duration of the start-up period; in the numerical simulations, we set $\tau = 0.1$. Three choices for the dimensionless function $g(x)$ are considered: the constant function $g(x) = 1$, the sinusoidal function $g(x) = \frac{1}{2}[1 - \cos(2\pi\hat{x})]$, and the quadratic function $g(x) = 16\hat{x}^2(1-\hat{x})^2$, where $\hat{x} \equiv x/L_x$. The third choice was employed by several previous authors [22,6,23]. The sinusoidal and quadratic functions prevent a velocity discontinuity from occurring at the upper corners of the cavity, and thereby allow for well-behaving numerical solutions.

The equation of motion was integrated in time using a finite-difference method implemented on a uniform non-staggered grid of size $N_x \times N_y$. In the fractional-step implementation, the convection–diffusion component equation (2.3) is split further into a convection–diffusion equation for the x direction and a convection–diffusion equation for the y direction (e.g., [24]),

$$\rho\left(\frac{\partial \mathbf{u}}{\partial t} + u_x\frac{\partial \mathbf{u}}{\partial x}\right) = \mu\frac{\partial^2 \mathbf{u}}{\partial x^2}, \qquad \rho\left(\frac{\partial \mathbf{u}}{\partial t} + u_y\frac{\partial \mathbf{u}}{\partial y}\right) = \mu\frac{\partial^2 \mathbf{u}}{\partial y^2}. \tag{3.2}$$

All spatial derivatives are approximated with second-order central differences with spacing $\Delta x = L_x/N_x$ and $\Delta y = L_y/N_y$, and time advancement is carried out by the fully-implicit Crank–Nicolson method, where the convection velocity multiplying the spatial derivatives on the left-hand sides of (3.2) is set equal to the solenoidal field at the beginning of the current step. The decomposition (3.2) is motivated by the fact that carrying out the individual x and y convection–diffusion steps requires solving systems of tridiagonal equations, which can be done efficiently using the Thomas algorithm. The projection step was implemented as shown in (2.12), and the projection function was computed by solving the Poisson equation (2.15).

Boundary conditions for the intermediate velocity include the no-penetration condition expressed by the first of Eqs. (2.5), and the slip condition

$$\mathbf{u}^* \cdot \mathbf{t} = \left(\mathbf{u}_B^{n+1} + \frac{\Delta t}{\rho}\nabla\phi^{n+1}\right) \cdot \mathbf{t}. \tag{3.3}$$

Because the second term on the right-hand side of (3.3) is not available during the convection–diffusion steps, it is approximated with the value at the previous step, and the approximation is improved by repeating the convection–diffusion steps after the projection step has been completed. Previous authors have shown that only one iteration is necessary to satisfy the no-slip

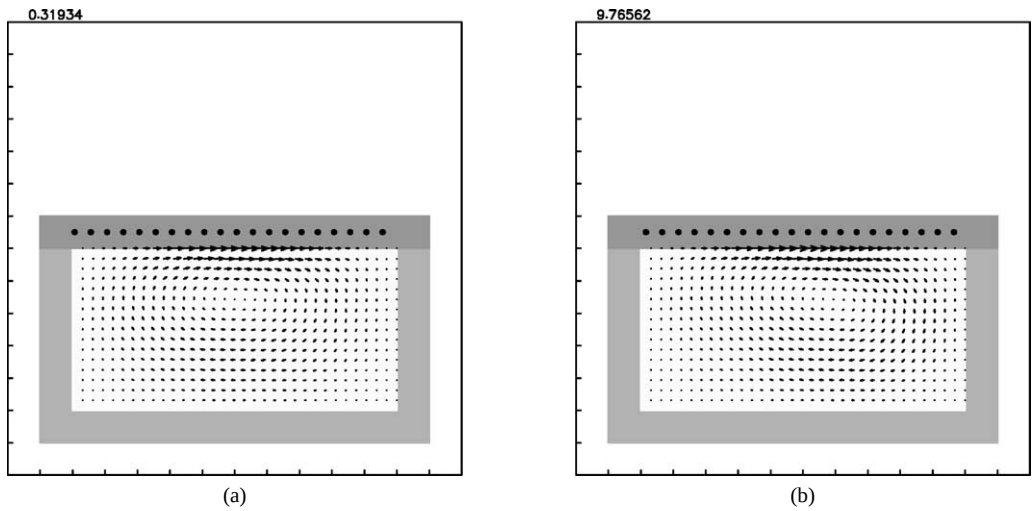

Fig. 1. Instantaneous velocity vector field of flow in a rectangular cavity with ramped sinusoidal lid velocity distribution for (a) $Re = 1$, and (b) 100, computed on a 32×16 grid. The label above each frame is the dimensionless time $\hat{t} \equiv Ut/L_x$ since the beginning of the motion.

boundary condition to second order in the time step [14]. Consistent with this result, we found only a few iterations are necessary for the magnitude of the slip velocity normalized by U to be reduced to 10^{-8}.

Now, because of the splitting of the x and y convection–diffusion steps and the fact that the convection velocity as well as the boundary velocity are held constant during each fractional step, the method is generally first-order accurate in Δt. However, when the boundary velocity is time independent and the Reynolds number is sufficiently small so that the nonlinear inertial term is negligible compared to the rest of the terms in the equation of motion, the method is of second order in time, corresponding to $\gamma = 1/2$. To see this, we consider the Crank–Nicolson discretized forms of (3.2),

$$\mathbf{u}' - \frac{1}{2}\nu\Delta t\frac{\partial^2\mathbf{u}'}{\partial x^2} = \mathbf{u}^n + \frac{1}{2}\nu\Delta t\frac{\partial^2\mathbf{u}^n}{\partial x^2}, \qquad \mathbf{u}^* - \frac{1}{2}\nu\Delta t\frac{\partial^2\mathbf{u}^*}{\partial y^2} = \mathbf{u}' + \frac{1}{2}\nu\Delta t\frac{\partial^2\mathbf{u}'}{\partial y^2}, \tag{3.4}$$

where a prime denotes the first intermediate velocity. Eliminating the first intermediate velocity yields

$$\mathbf{u}^* - \frac{1}{2}\nu\Delta t\nabla^2\mathbf{u}^* = \mathbf{u}^n + \frac{1}{2}\nu\Delta t\nabla^2\mathbf{u}^n + \frac{1}{4}(\nu\Delta t)^2\frac{\partial^4(\mathbf{u}^* - \mathbf{u}^n)}{\partial x^2\partial y^2}. \tag{3.5}$$

We note that the last fraction on the right-hand side is of order Δt, and recognize (3.5) as the approximate Crank–Nicolson factorization of (2.3) with the nonlinear inertia and body force term absent.

The Poisson equation for the projection function, Eq. (2.15), subject to the homogeneous Neumann boundary condition $\mathbf{n}\cdot\nabla\phi^{n+1} = 0$ originating from (2.6) was solved by Gauss–Seidel or SOR iterations implemented in two ways. In the first implementation, the Poisson equation is enforced at all interior and boundary finite-difference nodes, and phantom nodes are introduced to discretize the Neumann boundary condition using centered differences. The boundary distribution of the intermediate rate of expansion is computed by second-order one-sided differences. In the second implementation, the Poisson equation is enforced only at the interior nodes, and the Neumann boundary condition is implemented by one-sided second-order differences. In this case, the boundary distribution of the intermediate rate of expansion α^* is not required. The second version of the numerical method fails to capture with adequate resolution numerical boundary layers for the intermediate rate of expansion, and is somewhat inferior to the first choice, especially in the case of impulsively started motion.

The Gauss–Seidel and SOR iterations converge only when the solvability condition for the discrete Poisson–Neumann problem originating from the compatibility condition is fulfilled [25]. To ensure the satisfaction of this condition, the value of the projection function at the grid point located in the middle of the cavity is reset to the reference value of zero after a complete update. Doing this effectively adds a small homogeneous term to the source of the Poisson equation, thus balancing the boundary integrated outward flux.

The pressure Poisson equation subject to the Neumann boundary condition,

$$\mathbf{n}\cdot\nabla p = \mu\mathbf{n}\cdot\nabla^2\mathbf{u}, \tag{3.6}$$

was solved by similar methods. In particular, the left-hand side was approximated with central differences in the first implementation, and with second-order one-sided differences in the second implementation. Several methods of evaluating the right-hand side of (3.6) in terms of the discrete instantaneous velocity were implemented. Using the continuity equation, we derive the following finite-difference approximation at the lid grid points,

$$\frac{\partial p}{\partial y} = \mu\frac{\partial^2 u_y}{\partial y^2} \simeq \frac{4\mu}{\Delta y^2}\left[v_2 - \frac{1}{8}v_3 - \frac{3}{4}\Delta y\left(\frac{\partial u_x}{\partial x}\right)_{x,L_y}\right], \tag{3.7}$$

where $v_2 \equiv u_y(x, L_y - \Delta y)$ and $v_3 \equiv u_y(x, L_y - 2\Delta y)$. In the case of a rigid lid that translates with uniform velocity, the last term on the right-hand sides of (3.7) is absent. Alternative expressions based on first- and second-order backward difference approximations are

$$\frac{\partial p}{\partial y} \simeq \frac{\mu}{\Delta y^2}(-2v_2 + v_3), \qquad \frac{\partial p}{\partial y} \simeq \frac{\mu}{\Delta y^2}(-5v_2 + 4v_3 - v_4), \tag{3.8}$$

where $v_4 \equiv u_y(x, L_y - 3\Delta y)$. Similar expressions can be derived for the left, right, and bottom wall. Numerical experimentation has shown that the computed pressure field is sensitive to the implementation of the pressure Neumann boundary condition, especially at low Reynolds numbers where the pressure field is nearly harmonic. Best agreement between the computed pressure and the projection function was achieved with the finite-difference formula (3.7). All results presented in the next section were obtained using this choice.

The FORTRAN codes are available from the internet site http://stokes.ucsd.edu/pozrikidis/FDLIB/11_fdm/cvt_pm. A integrated graphics code that performs interactive animation on X11 systems based on the *vogle* library is available from the internet site http://stokes.ucsd.edu/pozrikidis/CFDLAB/11_fdm/cvt_pm.

4. Numerical results

As a benchmark, we consider flow in a rectangular cavity with depth to length ratio $L_y/L_x = 0.50$, subject to sinusoidal lid velocity distribution and ramped up motion, as discussed in Section 3. Fig. 1 shows the nearly steady instantaneous velocity vector field at Reynolds number $Re = 1$ and 100, computed on a 32×16 grid. The simulations were conducted using the first implementation of the numerical method discussed in Section 3, where Poisson's equation for the projection function is enforced at the interior as well as boundary nodes.

Our first goal is to confirm that the intermediate rate of expansion α^* exhibits the boundary-layer behavior discussed in Section 2. Fig. 2(a) shows the distribution of α^* nondimensionalized by U/L_x over the moving lid for $Re = 1$ near the steady state, computed with: (i) grid size $N_x = 16$, $N_y = 8$, and dimensionless time step $\Delta\hat{t} = 0.00390625$ (circles), (ii) $N_x = 32$, $N_y = 16$, $\Delta\hat{t} = 0.000976562$ (squares), and (iii) $N_x = 64$, $N_y = 32$, $\Delta\hat{t} = 0.00024414$ (diamonds). The most accurate computation with the finest grid up to dimensionless time $\hat{t} = 0.50$ requires 8 hours of CPU time on an INTEL 1.8 GHz processor running Linux. The results reveal that, as the time step is reduced by a factor of 4, the amplitude of the boundary distribution of α^* decreases by a factor of 2, in agreement with the theoretical predictions. In all three cases displayed in Fig. 2(a), the time step was selected so that the ratio of the numerical boundary-layer thickness to the grid spacing is $\delta/\Delta x \simeq (\nu\Delta t)^{1/2}/\Delta x = 1.0$. Consequently, the boundary layer is expected to extend roughly over one grid point away from each side. Fig. 2(b) shows a

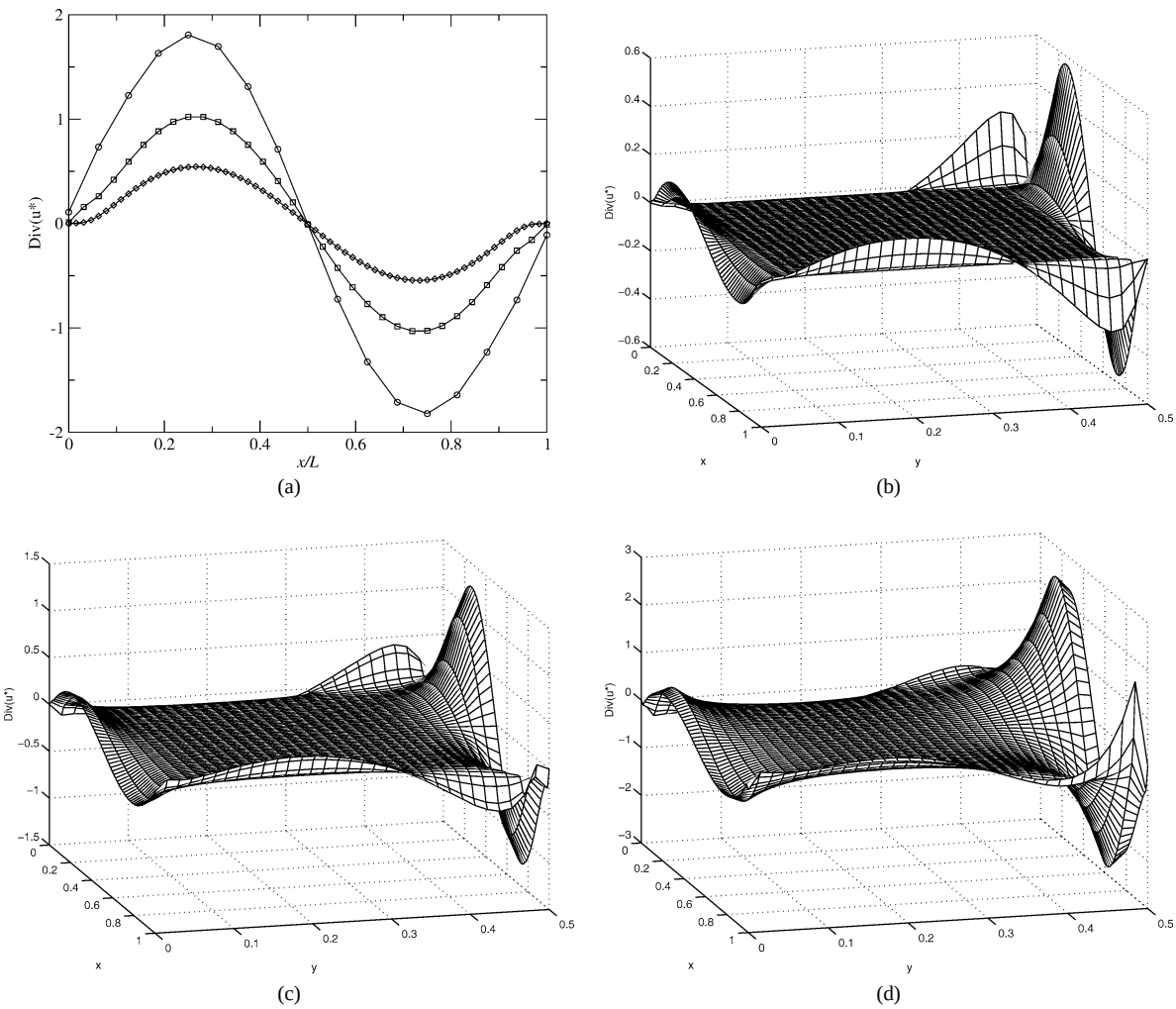

Fig. 2. Flow in a rectangular cavity with sinusoidal lid velocity distribution at $Re = 1$. (a) Distribution of the intermediate rate of expansion along the lid computed on a 16×8 (circles), 32×16 (squares), and 64×32 (diamonds) grid, with the time step adjusted so that the boundary layer thickness is equal to one grid spacing. (b) Distribution of the intermediate rate of expansion over the domain flow computed on the 64×32 grid, showing the boundary-layer behavior. (c) and (d) Same as (b), except that the time step is, respectively, 4 and 16 times as large.

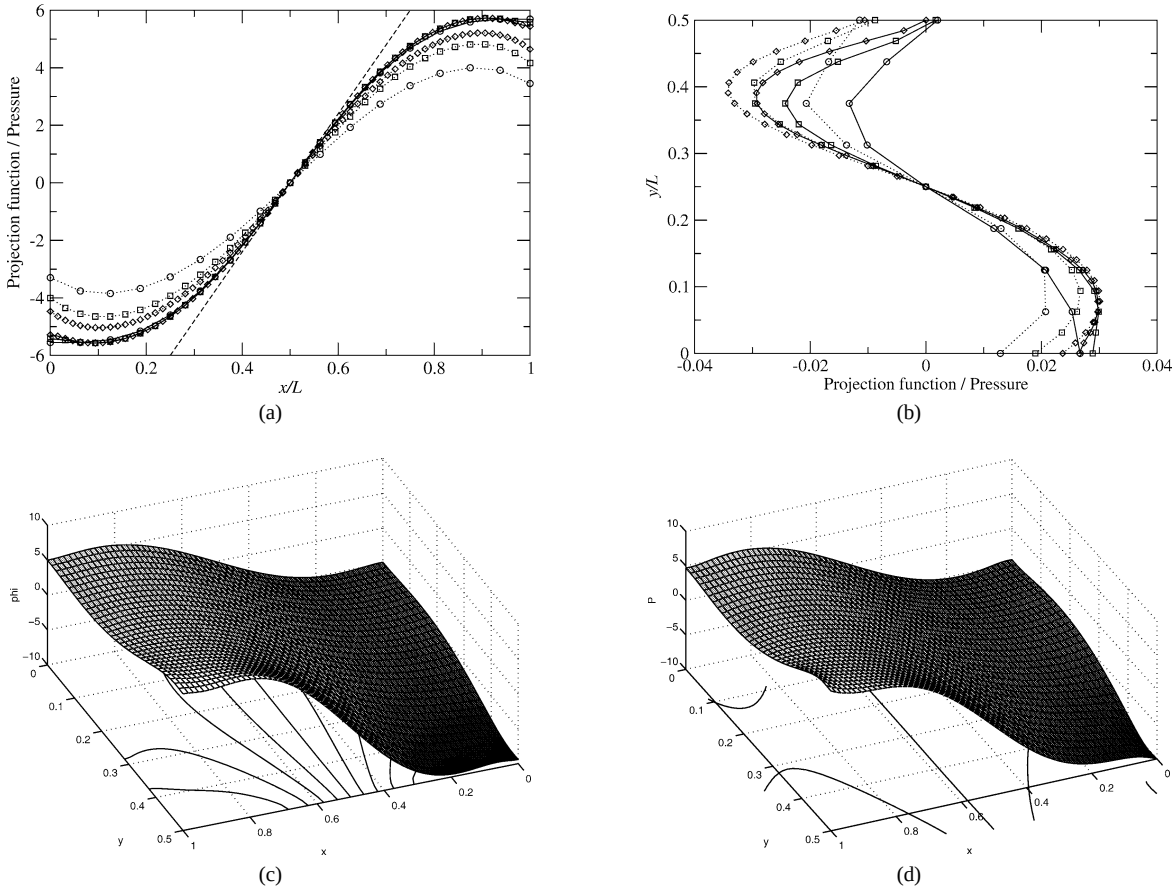

Fig. 3. Steady flow in a rectangular cavity with a sinusoidal lid velocity distribution at $Re = 1$. Distribution of the projection function (solid lines), and pressure (dotted lines) at the (a) horizontal, and (b) vertical mid-plane. The circles, squares, and diamonds correspond, respectively, to 16×8, 32×16, and 64×32 grid. (c) and (d) Distribution of the projection function and pressure.

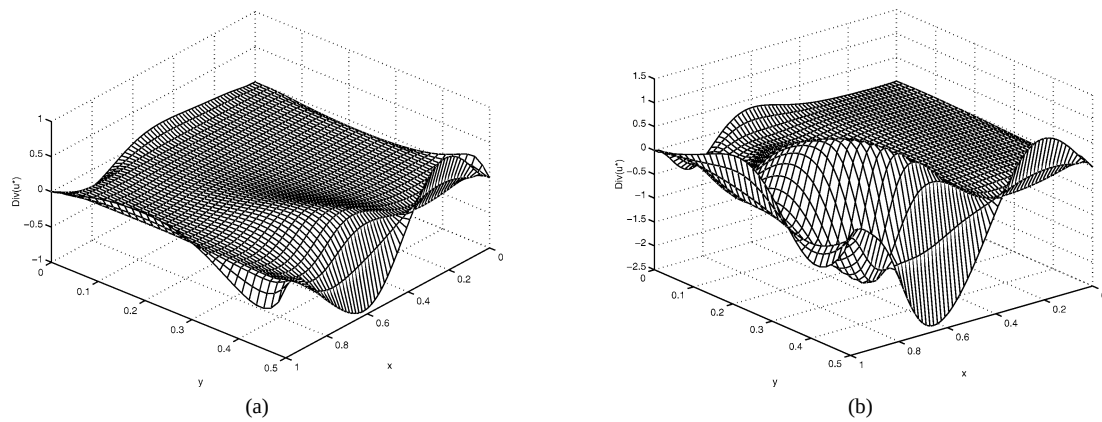

Fig. 4. Distribution of the intermediate rate of expansion near the steady state for flow in a rectangular cavity with sinusoidal lid velocity distribution at (a) $Re = 100$, and (b) 500.

three-dimensional graph of the distribution of the intermediate rate of expansion over the domain of flow computed on the 64×32 grid, confirming this theoretical prediction. Further support for the theoretical scaling is provided in the graphs shown in Fig. 2(c) and (d), which duplicate the graph shown in Fig. 2(b) except that the time step is, respectively, 4 and 16 times as large. As the time step is increased by a factor of 4 while the grid size is kept constant, the thickness of the numerical boundary

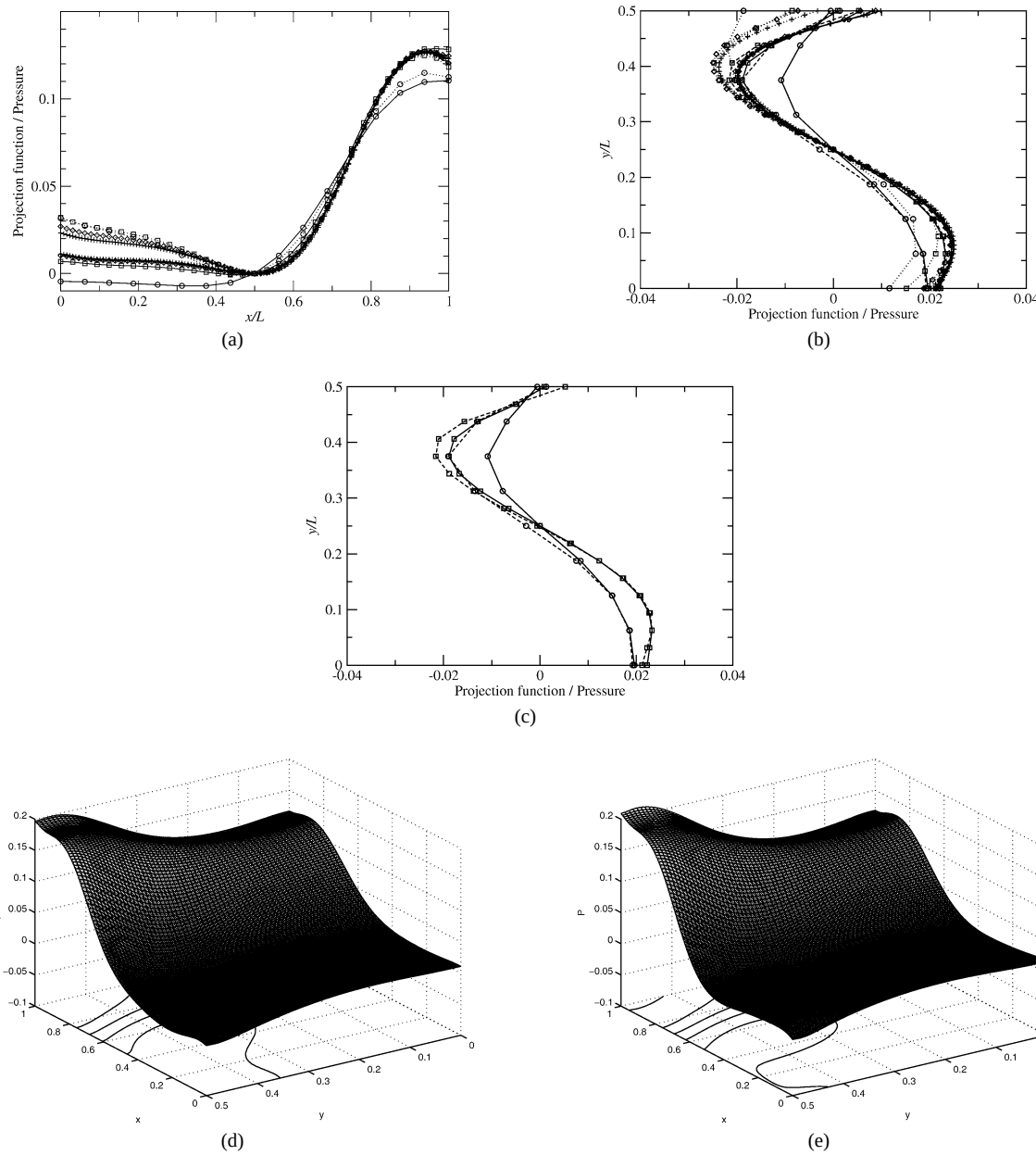

Fig. 5. Steady flow in a rectangular cavity with a sinusoidal lid velocity distribution at $Re = 1$. Distribution of the projection function (solid lines), and pressure (dotted lines) at the (a) horizontal, and (b) and (c) vertical mid-plane. The circles, squares, diamonds, and crosses correspond, respectively, to computations performed on a 16×8, 32×16, 64×32, and 128×64 grid. (d) and (e) Distribution of the projection function and pressure.

layer is doubled, that is, the boundary layer occupies twice as many grid spacings. Note that some irregularity of the boundary distribution of the intermediate rate of expansion begins setting when the time step exceeds a threshold, as shown in Fig. 2(d).

Next, we examine and compare the distributions of the projection function and pressure. Fig. 3(a) shows horizontal profiles of ϕ (solid lines) and p (dotted lines) at the mid-plane $y/L_y = 0.5$, and Fig. 3(b) shows vertical profile at the mid-plane $x/L_x = 0.5$, near the steady state. The circles, squares, and diamonds correspond, respectively, to the 16×8, 32×16, and 64×32 grid. In these and all subsequent graphs, the distributions of ϕ and p have been shifted so that they take the reference value of zero at the cavity mid-point $x/L_x = 0.5$, $y/L_y = 0.5$, and then reduced by the inertial scale ρU^2. The results confirm that, as the spatial discretization is refined, the distributions of ϕ and p converge to a common limit, although the rate of

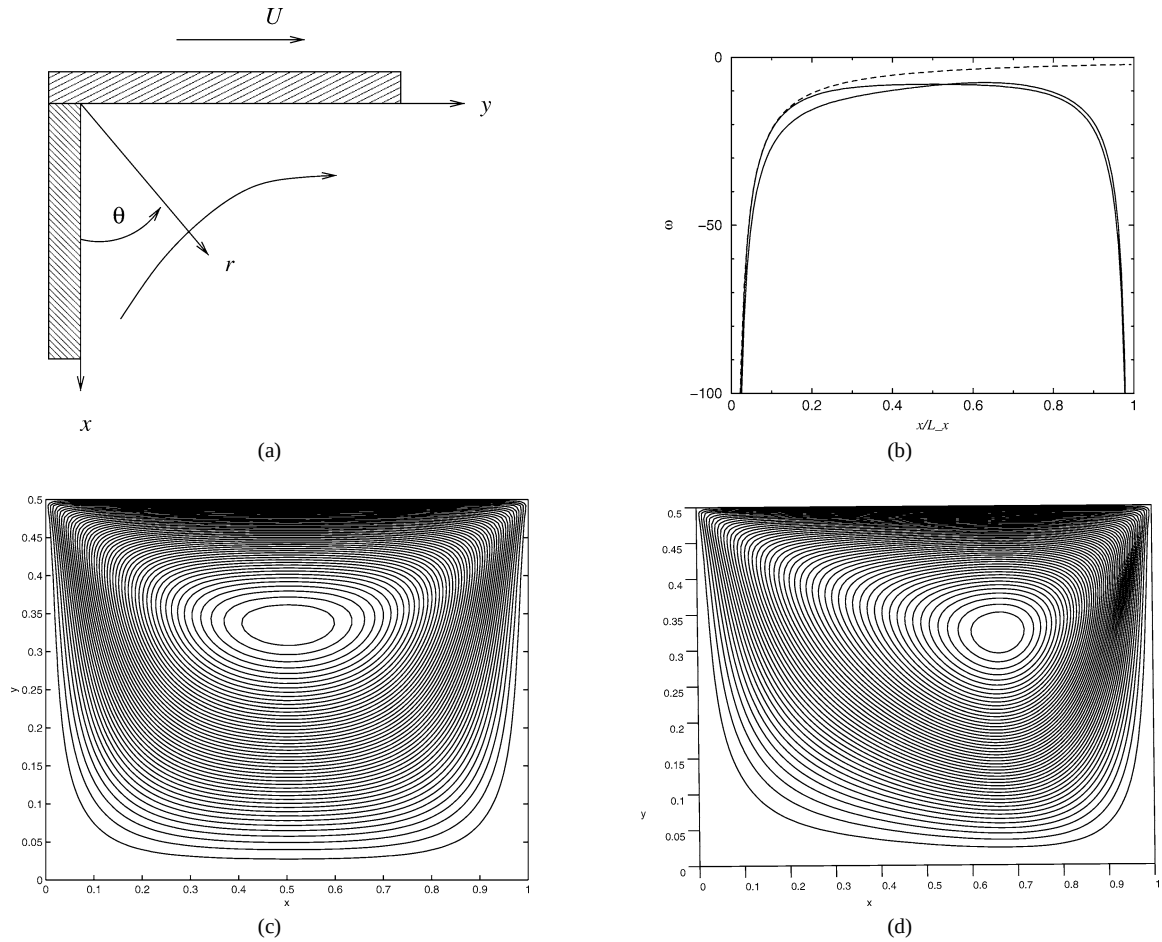

Fig. 6. Flow in a cavity driven by a translating rigid lid. (a) Local Cartesian coordinates and associated plane polar coordinates (r, θ) used to derive the local Stokes flow solution near the upper left corner. (b) Distribution of the vorticity over the lid for flow in a cavity with depth to length ratio 0.5, computed using the stream function/vorticity formulation on a 128×64 grid at $Re = 1$; the dashed line represents the theoretical predictions expressed by the second equation in (4.4). (c) and (d) Stream function contour plots for (c) $Re = 1$, and (d) 100.

convergence of the mildly varying vertical profile is slow especially near the stretching lid. Now, if the lid translated parallel to itself with uniform velocity U on a top of a slender cavity, a nearly unidirectional flow along the x axis with be established with a pressure gradient $\mathrm{d}p/\mathrm{d}x = 6\mu U/L_y^2$ that ensures the vanishing of the streamwise flow rate. This elementary prediction, represented by the dashed line in Fig. 3(a), is in surprisingly good agreement with the results of the numerical computation. Fig. 3(c) and (d) shows three-dimensional graphs of the projection function and pressure over the domain of flow computed with the finest discretization, demonstrating an overall good agreement.

Next, we examine the behavior in the presence of significant fluid inertia. Fig. 4 illustrates the distribution of the intermediate rate of expansion near the steady state for $Re = 100$ and 500, computed on the 64×32 grid with the time step adjusted so that $\delta/\Delta x = 1$. Comparing these distributions to that shown in Fig. 2(b) for $Re = 1$, we observe that, in addition to the boundary layers, significant intermediate compressibility develops throughout the domain of flow due to the inhomogeneous term on the right-hand side of (2.11).

Fig. 5(a) shows the horizontal profiles of ϕ (solid lines) and p (dotted lines) at the mid-plane $y/L_y = 0.5$, and Fig. 5(b) shows the corresponding vertical profiles at the mid-plane $x/L_x = 0.5$, near the steady state for $Re = 100$. The circles, squares, diamonds, and crosses correspond, respectively, to computations performed on a 16×8, 32×16, 64×32, and 128×64 grid. In all cases, the time step has been adjusted so that $\delta/\Delta x = 1$. Comparison of the graphs shown in Fig. 5(a) with those shown in Fig. 3(a) for $Re = 1$ shows that, as the Reynolds number is raised, the pressure distribution becomes unsymmetric with respect to the vertical mid-plane. The dashed lines in Fig. 5(b) trace the vertical profile of the projection function corrected according to (2.23) with $\gamma = 1/2$. For clarity, the profiles for the 16×8 and 32×16 grids are duplicated in Fig. 5(c). Although for the reasons discussed in Section 3 the adjustment is incomplete, the results show that the corrected distribution converges

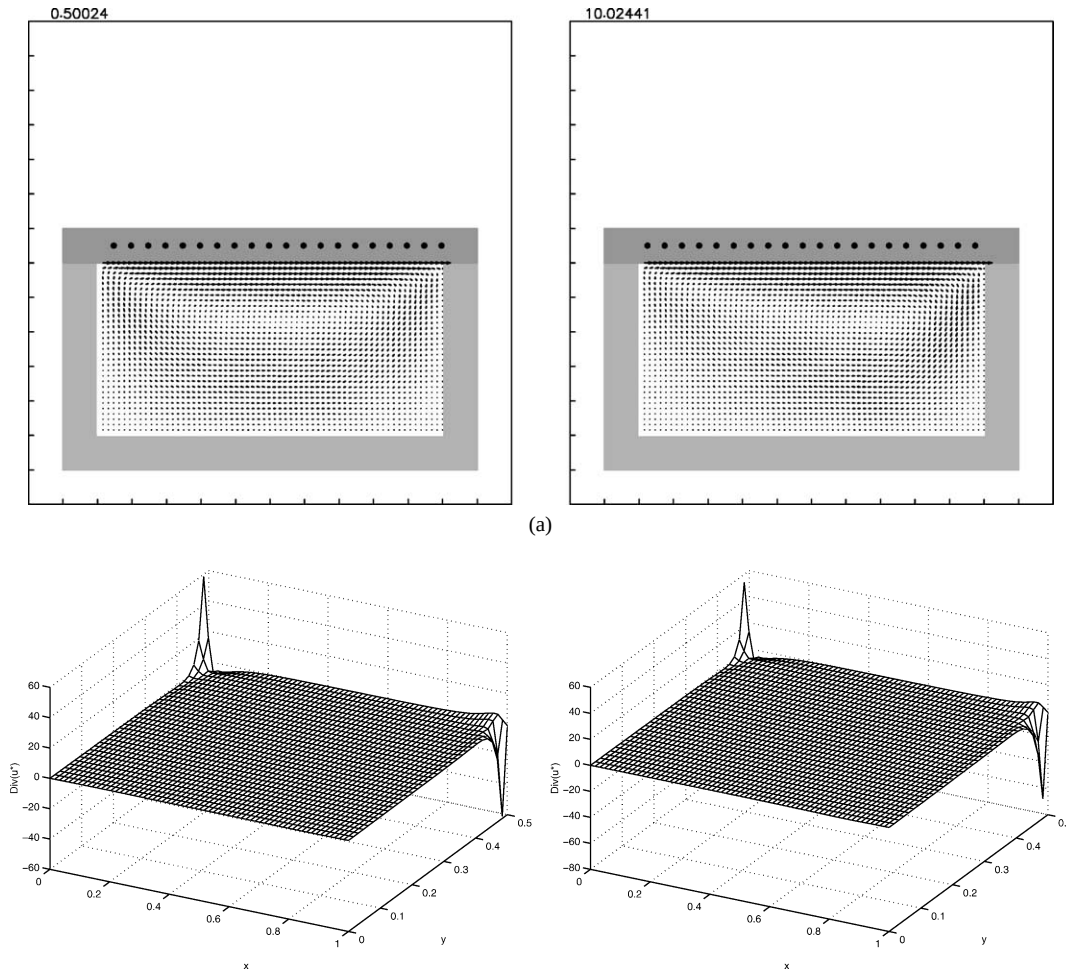

Fig. 7. Steady flow in a rectangular cavity with uniform lid velocity distribution at $Re = 1$ (left column) and 100 (right column). (a) Velocity vector field, (b) intermediate rate of expansion, (c) and (d) three-dimensional and contour plots of the projection function.

faster with respect to the level of discretization, and thereby improves the approximation to the pressure. Fig. 5(c) and (d) displays the distribution of the projection function and pressure over the domain of flow computed with the finest 128×64 grid, demonstrating a good overall agreement.

Next, we consider flow in a cavity driven by a rigid lid that translates parallel to itself with uniform velocity U. Viscous stresses dominate the force balance near the upper two corners where the boundary velocity is discontinuous at any Reynolds number. After transient start-up effects have disappeared, the local flow near the corners resembles Stokes flow in a quarter-plane bounded two semi-infinite orthogonally intersecting planes in relative motion. To describe the local flow, we introduce plane polar coordinates (r, θ) as illustrated in Fig. 6(a), and carry out a local analysis to find that, to leading order, the local stream function is given by [15]

$$\psi(r,\theta) \simeq \frac{4}{\pi^2 - 4} U r \Phi(\theta), \tag{4.1}$$

where

$$\Phi(\theta) \equiv \left(\frac{\pi}{2} - \theta\right) \sin\theta - \frac{\pi}{2}\theta\cos\theta. \tag{4.2}$$

The corresponding pressure field is given by

$$p(r,\theta) \simeq -\frac{8\mu}{\pi^2 - 4}\frac{U}{r}\left[\Phi'''(\theta) + \Phi'(\theta)\right] = -\frac{8\mu}{\pi^2 - 4}\frac{U}{r}\left(\frac{\pi}{2}\cos\theta + \sin\theta\right). \tag{4.3}$$

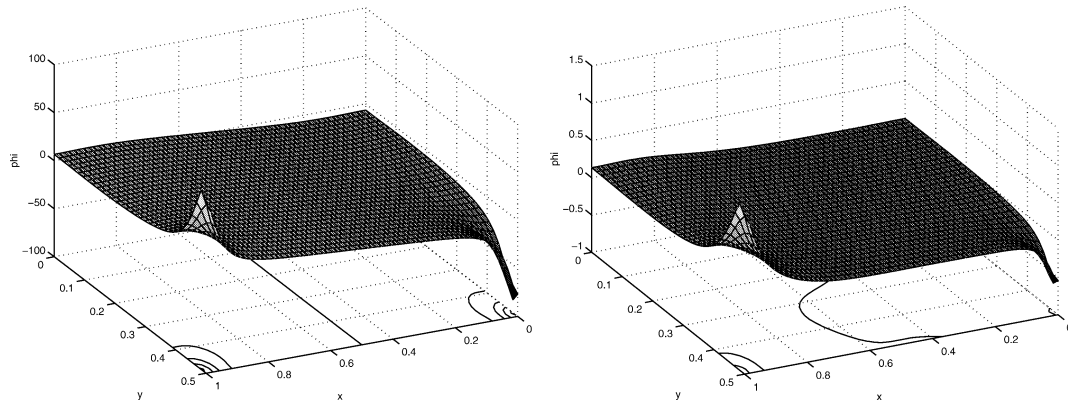

(c)

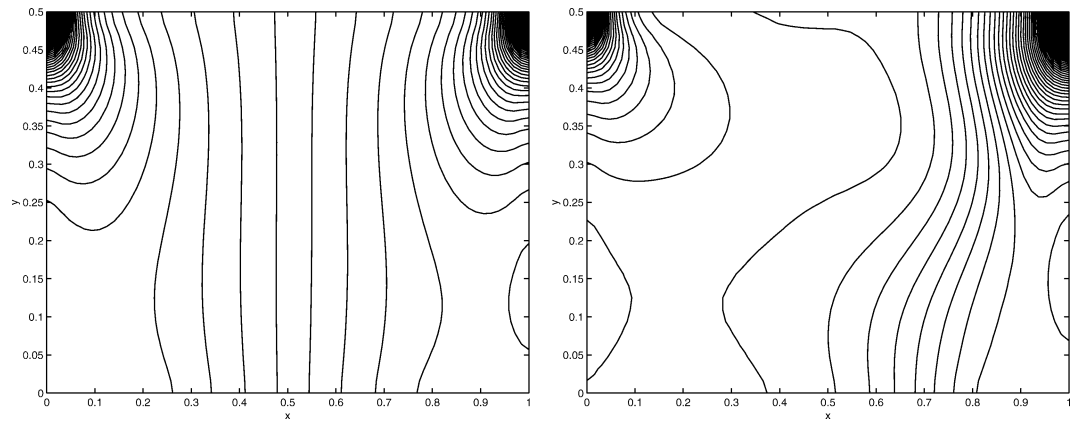

(d)

Fig. 7. (Continued.)

Expression (4.3) shows that the pressure exhibits a non-integrable singularity along the translating lid corresponding to $\theta = \pi/2$, as well as along the left wall corresponding to $\theta = 0$. The wall vorticity exhibits a similar non-integrable singularity,

$$\omega(r, \theta = 0) = -\frac{8}{\pi^2 - 4}\frac{U}{r}, \qquad \omega\left(r, \theta = \frac{\pi}{2}\right) = -\frac{4\pi}{\pi^2 - 4}\frac{U}{r}. \tag{4.4}$$

Locally near the corners, both pressure and vorticity are harmonic functions behaving like Green's function dipoles.

Previous authors have used the stream function/vorticity formulation to compute the *steady* flow by finite-difference methods. The numerical procedure involves making an initial guess for the vorticity field, solving a Poisson equation for the stream function subject to the homogeneous Dirichlet no-penetration boundary condition, and then solving a Poisson equation for the vorticity subject to a Dirichlet boundary condition that arises by simplifying the definition of the vorticity using the no-slip velocity boundary condition. The process is repeated until the computed vorticity field coincides with that originally assumed within a specified tolerance.

As a preliminary to discussing the performance of the projection method, we investigate the ability of the stream function/vorticity formulation to capture the singular behavior at the corners. A standard numerical method was implemented for this purpose involving second-order spatial differences for all derivatives involved in the governing equations and boundary conditions. The FORTRAN codes are available from the internet site http://stokes.ucsd.edu/pozrikidis/FDLIB/11_fdm/cvt_sv. A integrated graphics code that performs interactive animation on X11 systems based on the *vogle* library is available from the internet site http://stokes.ucsd.edu/pozrikidis/CFDLAB/11_fdm/cvt_sv. Fig. 6(c) and (d) shows stream function contour plots for flow in a cavity with aspect ratio $L_y/L_x = 0.5$, computed on a 128×64 uniform grid for $Re = 1$ and 100. The solid lines in Fig. 6(b) show the vorticity distribution along the lid for $Re = 1$ (thin line) and $Re = 100$ (heavy line). The dashed line represents the theoretical predictions expressed by the second equation in (4.4). The results reveal that the numerical method is remarkably efficient in capturing the boundary singularity almost all the way up to the corner.

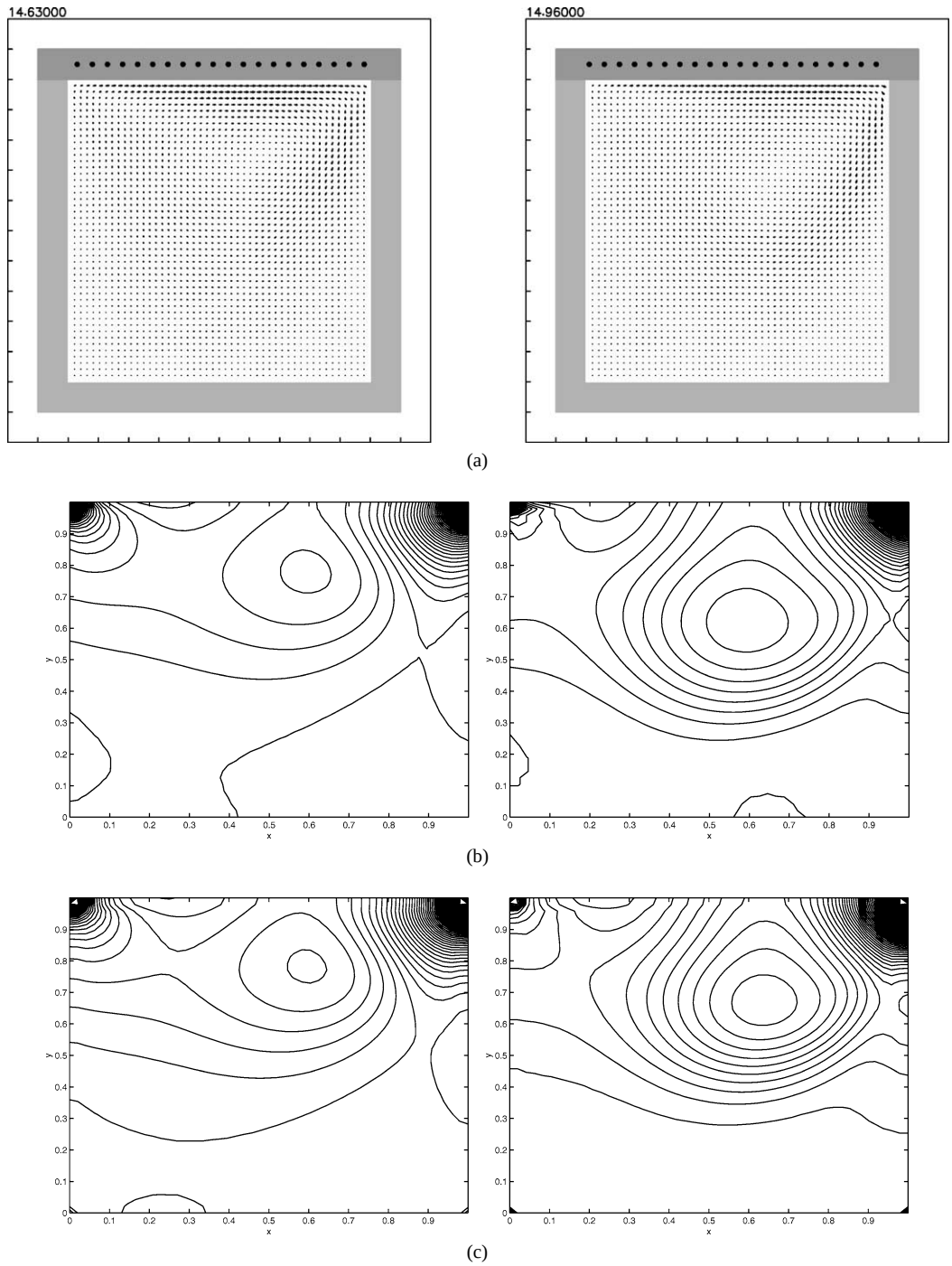

Fig. 8. Flow in a square cavity: (a) Velocity vector field, and distribution of the projection function obtained by the first (b) and second (c) implementation of the numerical method at Reynolds number $Re = 100$ (left) and 400 (right), computed on a 48×48 grid.

Turning now to the projection method, we observe that, because of the velocity discontinuity at the upper two corners, the intermediate rate of expansion exhibits a singular behavior. Fig. 7(a) shows velocity vector field near the steady state for $Re = 1$ (left) and 100 (right), and Fig. 7(b) shows the corresponding distributions of the intermediate rate of expansion. These computations were carried out using the first implementation of the numerical method discussed in Section 3 on a 64×32 grid, where the Poisson equation is enforced at the interior and boundary nodes, and the time step is adjusted so that $\delta/\Delta x = 1$.

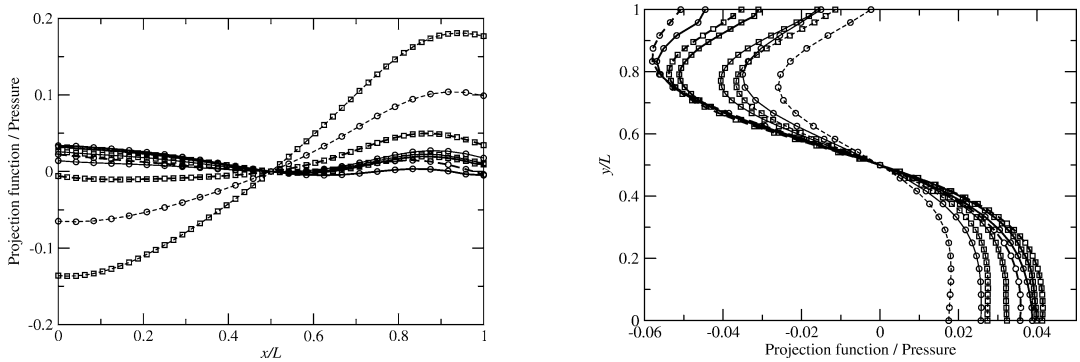

Fig. 9. Flow in a square cavity: (a) horizontal, and (b) vertical profiles of the projection function (solid lines) and pressure (dashed lines) for the first (thin lines) and second (thick lines) implementation.

Similar results were obtained with the second implementation. The results suggest that the singular behavior of the rate of expansion at the upper two corners does not have a catastrophic effect on its overall distribution far from the corners.

Fig. 7(c) and (d) shows three-dimensional and contour plots of the projection function, which was confirmed to converge as the grid size is refined. In contrast, extensive numerical experimentation revealed that obtaining an accurate solution of the Poisson equation for the pressure using the first or second implementation of the numerical method discussed in Section 3 is frustrated by the strong $1/r$ corner singularity and the even stronger $1/r^2$ singularity of its normal derivative, evident from the local solution (4.3). In particular, we found that the computed pressure field is notably sensitive to the grid size and method of implementing the inhomogeneous Neumann boundary condition.

Similar behavior was observed for cavities with different aspect ratios. For example, Fig. 8(a) displays the nearly steady velocity vector field for flow in a square cavity at Reynolds number $Re = 100$ (left) and 400 (right), computed on a 48×48 grid, and Fig. 8(b) and (c) displays three-dimensional graphs of the projection function computed with (b) the first, and (c) second implementation of the numerical method. In spite of the strong corner singularities, the general features of the distribution are consistently produced by both approaches. To convey a quantitative assessment of the performance of the numerical methods, in Fig. 9 we present mid-plane (a) horizontal, and (b) vertical profiles of the projection function (solid lines) and pressure (dashed lines) for grid size 24×24 (circles) and 48×48 (squares). The thin lines correspond to the first implementation, and the thick lines correspond to the second implementation. The irregular behavior of the pressure field is particularly evident in the horizontal profiles shown in (a).

5. Discussion

The numerical results presented in this paper suggest that the solution of the Poisson equation for the projection function using finite-difference methods on non-staggered grids subject to the homogeneous Neumann boundary condition is reliable even in the presence of boundary singularities. In contrast, when the boundary velocity is discontinuous, the numerical solution of the pressure is frustrated by the singular behavior of the normal derivative.

Several previous authors computed the pressure field of flow in a cavity driven by a translating rigid lid on non-staggered grids. Burggraf [26] generated the pressure field of the steady flow by integrating in space the equation of motion after the velocity field has been computed using the stream function/vorticity formulation, thereby circumventing the numerical solution of the pressure Poisson equation. Ghia et al. [27,28] used a finite-difference method similar to that implemented in the present work, and reported that an alternative implementation that does not enforce the pressure Poisson equation at the boundary nodes but at an unspecified interior boundary is more satisfactory. It is not clear from their discussion how the time derivative $\partial \mathbf{u}/\partial t$ involved in the pressure Neumann boundary condition at the interior boundary is evaluated. If this term is set equal to zero, then the method is exact only in the case of steady flow. The pressure contour plots presented by Ghia et al for steady flow are similar to those for the projection function displayed in Fig. 8 of this paper.

Abdallah, Mansour and Hamed [29–31] developed consistent finite difference methods on non-staggered Cartesian and curvilinear grids, where the satisfaction of the solvability condition for the pressure Poisson equation is embedded in the discretization. In this formulation, the Neumann boundary condition is effectively applied mid-way between the boundary and adjacent grid plane, and the time derivative of the velocity is set equal to zero. Babu and Korpela [32] pointed out that this is permissible only in the case of steady flow. We have modified the second implementation of the numerical method discussed in

Section 3 to enforce the Neumann boundary condition at the mid-point, using central differences to approximate all derivatives involved in the projected equation of motion for steady flow. Although this modification improved somewhat the agreement between the projection function and the pressure, significance discrepancies ad slow convergence still persisted in the case of flow induced by a translating rigid lid.

Other authors have published pressure fields of the rigid-lid driven-cavity flow using finite difference methods on staggered grids that account for the Neumann boundary condition implicitly through the reflected velocity boundary condition [33,31], finite-volume methods [34], and finite-element methods [35]. The success of these methods must be attributed, in part, to the fact that the compatibility condition condition for the Poisson equation is automatically satisfied. In particular, in the finite-volume and finite-element methods, the corner singularities are masked by the area or volume integration inherent in the finite-volume or Galerkin projection.

References

[1] A. Chorin, Numerical solution of the Navier–Stokes equations, Math. Comp. 22 (1968) 745–762.
[2] A. Chorin, On the convergence of discrete approximations to the Navier–Stokes equations, Math. Comp. 23 (1969) 341–353.
[3] P.M. Gresho, On the theory of semi-implicit projection methods for viscous incompressible flow and its implementation via a finite-element method that also introduces a nearly consistent mass matrix. Part 1: Theory, Int. J. Numer. Methods Fluids 11 (1990) 587–620.
[4] G.E. Karniadakis, M. Israeli, S.A. Orszag, High-order splitting methods for incompressible Navier–Stokes equations, J. Comput. Phys. 97 (1991) 414–443.
[5] W. Heinrichs, Splitting techniques for the pseudospectral approximation of the unsteady Navier–Stokes equations, SIAM J. Numer. Anal. 30 (1993) 19–39.
[6] S. Hugues, A. Randriamampianina, An improved projection scheme applied to pseudospectral methods for the incompressible Navier–Stokes equations, Int. J. Numer. Methods Fluids 28 (1998) 501–521.
[7] W. Heinrichs, Splitting techniques for the unsteady Stokes equations, SIAM J. Numer. Anal. 35 (1998) 1646–1662.
[8] G.E. Karniadakis, S.J. Sherwin, Spectral/hp Element Methods for CFD, Oxford University Press, New York, 1999.
[9] H. Haschke, W. Heinrichs, Splitting techniques with staggered grids for the Navier–Stokes equations in the 2D case, J. Comput. Phys. 168 (2001) 131–154.
[10] J. Kim, P. Moin, Application of a fractional step method to incompressible Navier–Stokes equations, J. Comput. Phys. 59 (1985) 308–323.
[11] R. Temam, Remark on the pressure boundary condition for the projection method, Theoret. Comput. Fluid Dynamics 3 (1991) 181–184.
[12] J.B. Perot, An analysis of the fractional step method, J. Comput. Phys. 108 (1993) 51–58.
[13] J.C. Strikwerda, Y.S. Lee, The accuracy of the fractional step method, SIAM J. Numer. Anal. 37 (1999) 37–47.
[14] D.L. Brown, R. Cortez, M.L. Minion, Accurate projection methods for the incompressible Navier–Stokes equations, J. Comput. Phys. 168 (2001) 464–499.
[15] C. Pozrikidis, Introduction to Theoretical and Computational Fluid Dynamics, Oxford University Press, New York, 1997.
[16] R. Rannacher, On Chorin's projection method for the incompressible Navier–Stokes equations, in: Heywood, et al. (Eds.), The Navier–Stokes equations II – Theory and Numerical Methods, in: Lecture Notes in Math., Springer-Verlag, Berlin, 1991.
[17] W. E, J.-G. Liu, Projection method I: Convergence and numerical boundary layers, SIAM J. Numer. Anal. 32 (1995) 1017–1057.
[18] S.A. Orszag, M. Israeli, M.O. Deville, Boundary conditions for incompressible flows, J. Sci. Comput. 1 (1986) 75–111.
[19] M.J. Lee, B.D. Oh, Y.B. Kim, Canonical fractional-step methods and consistent boundary conditions for the incompressible Navier–Stokes equations, J. Comput. Phys. 168 (2001) 73–100.
[20] N.N. Yanenko, The Method of Fractional Steps for Solving Multi-Dimensional Problems of Mathematical Physics in Several Variables, Springer, New York, 1971.
[21] F. Sotiropoulos, S. Abdallah, The discrete continuity equation in primitive variable solutions of incompressible flow, J. Comput. Phys. 95 (1991) 212–227.
[22] R. Peyret, D. Taylor, Computational Methods for Fluid Flow, Springer-Verlag, New York, 1983.
[23] J. Shen, Hopf bifurcation of the unsteady regularized driven cavity flow, J. Comput. Phys. 95 (1991) 228–245.
[24] K. Goda, Multistep technique with implicit difference schemes for calculating two- and three-dimensional cavity flows, J. Comput. Phys. 30 (1979) 76–95.
[25] C. Pozrikidis, A note on the regularization of the discrete Poisson–Neumann problem, J. Comput. Phys. 172 (2001) 1917–1923.
[26] O.R. Burggraf, Analytical and numerical studies of the structure of steady separated flows, J. Fluid Mech. 24 (1966) 113–151.
[27] K.N. Ghia, W.L. Hankey Jr., J.K. Hodge, Study of incompressible Navier–Stokes equations in primitive variables, AIAA paper 77-648, 1977, pp. 156–165.
[28] K.N. Ghia, W.L. Hankey Jr., J.K. Hodge, Use of primitive variables in the solution of incompressible Navier–Stokes equations, AIAA J. 17 (1979) 298–301.
[29] S. Abdallah, Numerical solutions for the pressure Poisson equation with Neumann boundary conditions using a non-staggered grid, I, J. Comput. Phys. 70 (1987) 182–192.
[30] S. Abdallah, Numerical solutions for the incompressible Navier–Stokes equations in primitive variables using a non-staggered grid, II, J. Comput. Phys. 70 (1987) 193–202.
[31] M.L. Mansour, A. Hamed, Implicit solution of the incompressible Navier–Stokes equations on a non-staggered grid, J. Comput. Phys. 86 (1990) 147–167.

[32] V. Babu, S.A. Korpela, Numerical solution of the incompressible, three-dimensional Navier–Stokes equations, Comput. Fluids 23 (1994) 675–691.
[33] K. Gustafson, K. Halasi, Vortex dynamics in cavity flows, J. Comput. Phys. 64 (1986) 279–319.
[34] R. Klein, N. Botta, T. Schneider, C.D. Munz, S. Roller, A. Meister, L. Hoffmann, T. Sonar, Asymptotic adaptive methods for multi-scale problems in fluid mechanics, J. Engrg. Math. 39 (2001) 261–343.
[35] P.M. Gresho, S.T. Chan, R.E. Lee, C.D. Upson, A modified finite-element method for solving the time-dependent incompressible Navier–Stokes equations. Part 2: Applications, Int. J. Numer. Methods Fluids 4 (1984) 619–640.